RESEARCH ARTICLE



Shallow Katabatic Flow in a Complex Valley: An Observational Case Study Leveraging Uncrewed Aircraft Systems

Sean C. C. Bailey¹ • Suzanne Weaver Smith¹ • Michael P. Sama² • Loiy Al-Ghussain¹ • Gijs de Boer^{3,4,5}

Received: 20 July 2022 / Accepted: 28 December 2022 / Published online: 20 January 2023 © The Author(s), under exclusive licence to Springer Nature B.V. 2023

Abstract

Multiple fixed-wing and multirotor uncrewed aircraft systems were deployed to measure the early morning katabatic flow along a valley as part of the lower atmosphere profiling studies at elevation a remotely-piloted aircraft team experiment (LAPSE-RATE) campaign. The valley's topography was that of a narrow canyon emerging into a broader shallow-sloped valley, allowing for an assessment of the suitability of one-dimensional approximations for the broad, flat part of the valley. The one-dimensional integral model predicts growth in the katabatic layer with downslope distance, which was not observed in the broader portions of the valley. Instead, observations revealed thinning of the katabatic layer at the valley centreline, coinciding with oscillatory behavior with a period between 30 and 60 min. These features were attributed to strong asymmetry and three-dimensional features initiating in the narrow part of the valley. These features produced initial conditions upstream of the broad slope flow that were not captured by the one-dimensional model.

Keywords Cold-air drainage · Topographic impact · Uncrewed aircraft systems (UAS) · Valley flows · Katabatic flow

This work was supported by the US National Science Foundation through Award No. CBET-1351411 and by Award No. 1539070, Collaboration Leading Operational UAS Development for Meteorology and Atmospheric Physics (CLOUDMAP). Additional support was provided by the US National Science Foundation (AGS 1807199), US Department of Energy (DE-SC0018985), and the NOAA Physical Sciences Laboratory. The authors would also like to acknowledge Dr. Julie Lundquist and her students Camden Plunkett and Patrick Murphy from University of Colorado Boulder who collected and provided the lidar data used in this study.

Integrated Remote and In Situ Sensing, University of Colorado Boulder, Boulder CO 80309, USA



Sean C. C. Bailey sean.bailey@uky.edu

Department of Mechanical and Aerospace Engineering, University of Kentucky, Lexington, KY 40506, USA

Department of Biosystems and Agricultural Engineering, University of Kentucky, Lexington, KY 40506, USA

Cooperative Institute for Research in Environmental Sciences, University of Colorado Boulder, Boulder, CO 80309, USA

NOAA Physical Sciences Laboratory, Boulder, CO 80305, USA

1 Introduction

Thermally-induced gravity-driven katabatic (downslope) and anabatic (upslope) flows can have a significant impact on near-surface processes, especially where mountain valleys and basins interact. For example, drainage basin air currents and agricultural production, airborne material transport and dispersion (Orgill and Schreck 1985), aviation valley fog forecasting (Pilie et al. 1975), urban air quality (Fernando and Pardyjak 2013), in addition to renewable energy generation (Clifton et al. 2014) and wildfire spread (Wagenbrenner et al. 2016), are all affected by these phenomena. As a result, these types of flows have been studied for decades, (e.g. Defant 1951; Zardi and Whiteman 2013).

Nighttime formation of density gradients results in katabatic flows in mountain valleys, driving cold-air longitudinal (down-valley) drainage flows along the sloping valley floor. After sunrise, solar heating of the sloped valley sidewalls can induce up-wall vertical motions, initiating cross-sectional currents that persist until the longitudinal winds turn up-valley with the reversal of the density gradients. In general, the morning erosion of katabatic flow is seen in a lowering of the top of the drainage layer current, combined with the development of a convective mixing layer (Ayer 1961). Observations suggest such a transition can occur along the slope prior to reaching the end of the slope, with the location of transition depending on the details of the topography and its receptivity to surface heating (Papadopoulos and Helmis 1999). In complex terrain, this process can also be related to upslope flow intruding on the downslope cold pool (Princevac and Fernando 2008).

Complicating the understanding of katabatic winds and drainage flows is the complex structure of the developing winds, dependent on the slope of the valley (Grisogono and Axelsen 2012) with even simple shallow valleys vulnerable to transient disruptions (Mahrt et al. 2014). Furthermore, these flows are potentially highly three-dimensional due to coupling of the sidewall slope winds with the down-valley winds and conditions at the outlet of the valley (Ayer 1961; Clements et al. 1989b; Doran et al. 1990). Additional asymmetries in the cross-valley currents are noted when topology or external weather influence the valley drainage flow. Hence, valley geometry (Sakiyama 1990), soil moisture and evaporation dynamics (Hang et al. 2016), and forest canopy (Pypker et al. 2007) can impact the drainage flow and corresponding events, for example as CO₂ advection from a watershed (Pypker et al. 2007; Sun et al. 2010). In addition, external mesoscale atmospheric influences may cause counterintuitive afternoon down-valley winds (Banta and Cotton 1981), cross-valley drainage disruptions (Barr and Orgill 1989), multi-valley variability (Orgill et al. 1992), mountain wave katabatic interaction (Poulos et al. 1999, 2007), or lee wave resonant amplification (Pattantyus et al. 2011), among other effects.

These complex interconnections create a complicated highly turbulent environment which confounds simple eddy-viscosity and eddy-diffusivity modeling (Grisogono et al. 2015). Despite efforts to simulate and observe these circulations, the overall understanding of katabatic winds and drainage flows has been inadequate to develop subgrid-scale parameterizations which allow refinement of resolutions for advanced numerical weather prediction (Grisogono et al. 2015). For example, large-eddy simulations (LES) demonstrate discrepancies in momentum flux, buoyancy flux and turbulence production (Axelsen and van Dop 2009a, b) depending on the turbulence parameterization employed by the model (Grisogono et al. 2015). In addition, non-local effects introduced by features such as Kelvin–Helmholtz waves and advected turbulent mixing can impact the accuracy of surface parameterizations (Pinto et al. 2006).



Large field experiments investigating katabatic flows include Atmospheric Studies in Complex Terrain (ASCOT) (Orgill and Schreck 1985; Clements et al. 1989b; Barr and Orgill 1989; Gudiksen 1989; Leone and Lee 1989; Clements et al. 1989a), the Vertical Transport and Mixing Experiment (VTMX) (Monti et al. 2002), the COLd-air Pooling Experiment (COLPEX) modeling project and field experiment (Price et al. 2011), and the Mountain terrain Atmospheric Modeling and Observations program (MATERHORN) (Fernando and Pardyjak 2013; Fernando et al. 2015; Di Sabatino 2016; Hang et al. 2016). MATERHORN first integrated fixed-wing uncrewed aircraft system (UAS) platforms to support the collection of observations to help answer questions related to the complex set of relationships outlined above. The use of these systems, and their ability to capture high resolution three-dimensional features of valley cold-air drainage was further explored in the 2018 Lower Atmosphere Profiling Studies at Elevation—a Remotely-piloted Aircraft Team Experiment (LAPSE-RATE) (de Boer et al. 2020a), which featured the simultaneous deployment of tens of UAS in and around the northern San Luis Valley of Colorado.

UAS- and surface-based data sets from LAPSE-RATE are available as a collection (e.g. de Boer et al. 2020b; Bailey et al. 2020, and others). Here, we present a detailed analysis of a subset of the measurements obtained from the morning of 19 July, when measurement assets were deployed to measure the morning transition of cold-air drainage flow into the San Luis Valley, and demonstrate the viability of using UASs to extract highly resolved, three-dimensional information about the katabatic flow. Of interest in this paper is the measured behavior of the flow in a broad portion in a portion of the Saguache Valley which feeds into the San Luis Valley. This portion of the valley is geometrically similar to idealized slope flow, and we examine the flow in the broadening Saguache valley in the framework of canonical shallow slope flow as modeled by one-dimensional integral equations (e.g. Manins and Sawford 1979). In Sect. 2, we review the one-dimensional. In Sect. 3, the valley, measurement equipment and observational approach is described. In Sect. 4, we investigate how the katabatic flow over a shallow slope develops from the complex valley, and how the inflow conditions introduce three-dimensionality that is not accounted for in the one-dimensional model. These observations are summarized in Sect. 5.

2 One-Dimensional Model for Katabatic Flow

Katabatic flows on planar slopes in wide valleys can be idealized as being two-dimensional, with geometry as shown in Fig. 1, and are generally expected to be governed by the balance between mass, momentum and energy as expressed through integral forms of the equations of motion (Manins and Sawford 1979; Papadopoulos et al. 1997; Haiden and Whiteman 2005; Princevac et al. 2008). These equations assume negligible Coriolis effects and that the katabatic flow takes the form of a perturbation from an undisturbed state. The nocturnal cooling produces a potential temperature perturbation, δ , where δ is a function of downslope coordinate, s, downslope normal coordinate, n, and time, t, and is defined as:

$$\delta(s, n, t) = \theta_{va} - \theta_{v}. \tag{1}$$

Here θ_v is virtual potential temperature of the katabatic flow, and θ_{va} is the corresponding undisturbed profile, assumed to take the form:

$$\theta_{vq} = \theta_{vR} + \gamma z : \tag{2}$$



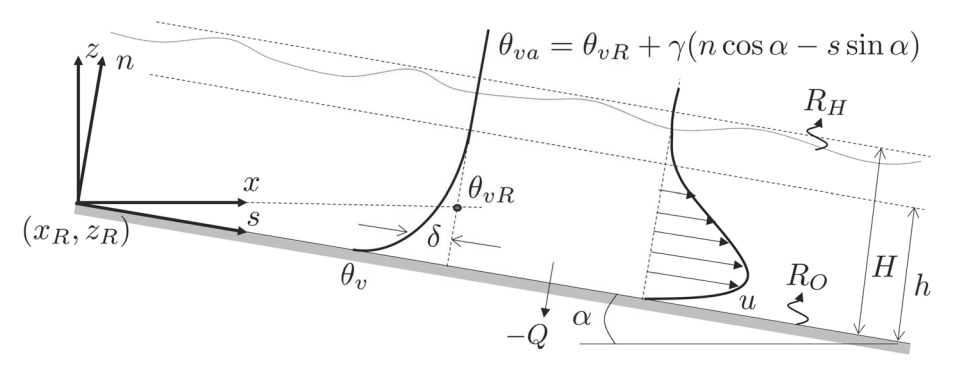


Fig. 1 Schematic of idealized stably stratified katabatic flow illustrating coordinate system and nomenclature used

or:

$$\theta_{va} = \theta_{vR} + \gamma (n\cos\alpha - s\sin\alpha) : \tag{3}$$

Here, γ is the ambient virtual potential temperature gradient, z is the vertical direction, opposite to gravitational acceleration, g, and θ_{vR} is a reference virtual potential temperature (e.g. the temperature at z=0). Note that s and n are rotated by an angle α from x and z as illustrated in Fig. 1, such that $z=n\cos\alpha-s\sin\alpha$ and $x=s\cos\alpha+n\sin\alpha$.

Unperturbed and perturbed buoyancy can then be defined as:

$$b_{va} = g\gamma (n\cos\alpha - s\sin\alpha)/\theta_{vR} : (4)$$

$$b_v = [g\gamma(n\cos\alpha - s\sin\alpha) - \delta]/\theta_{vR},\tag{5}$$

leading to:

$$b = b_v - b_{va} : (6a)$$

$$= -g\delta/\theta_{vR} \tag{6b}$$

$$= -g', (6c)$$

where g' is the reduced gravity. Finally, the buoyancy frequency can be defined as:

$$N^2 = g\gamma/\theta_{vR} : (7)$$

$$= db_{va}/dz. (8)$$

As detailed in Manins and Sawford (1979), assuming a two-dimensional katabatic flow, the momentum and buoyancy (energy) equations can be integrated across the layer depth, H, in the n direction to produce corresponding one-dimensional forms of:

$$\frac{\partial Uh}{\partial t} + \frac{\partial U^2h}{\partial s} = -\frac{\partial}{\partial s} \left(\frac{1}{2} S_1 \Delta h^2 \cos \alpha \right) + S_2 \Delta h \sin \alpha - C_D U^2 - \overline{u'w'}|_H : \tag{9}$$

and:

$$\frac{\partial}{\partial t} (S_2 \Delta h) + UhN^2 (\sin \alpha - S_3 E \cos \alpha) + \frac{\partial}{\partial s} (U \Delta h) = B_0 - \overline{g'w'}|_H : . \tag{10}$$

Introduced through this averaging process are the surface drag coefficient, $C_D = -\overline{u'w'}|_0/U^2$, used to approximate the Reynolds shear stress at the surface, with the corresponding stress at the edge of the katabatic layer being $-\overline{u'w'}|_H$. E is an entrainment



coefficient which can be approximated by the entrainment law E = A/(k+Ri) where A and k are constants (following Manins and Sawford (1979) and Princevac et al. (2008)) and Ri is the Richardson number. Corresponding sensible heat flux stresses are $-\overline{\theta_v'w'}|_H$ and $-\overline{\theta_v'w'}|_0$ with the former being expressed as $\overline{g'w'}$ and the latter being included in 10 through:

$$B_0 = g \frac{(R_H - R_0) - \rho C_P \overline{u'\theta_v'}|_0}{\rho_R C_P \theta_{vR}} :$$
 (11)

which also introduces the radiation flux divergence across H, $(R_H - R_0)$. Also introduced is the surface heat flux $Q = \rho C_p \overline{\theta_n' w'}|_0$.

In 9 and 10, U, h and Δ are the characteristic scales of downslope velocity, layer thickness and buoyancy deficit, respectively. These quantities are found from:

$$Uh = \int_0^H u \, \mathrm{d}n : \tag{12a}$$

$$U^2h = \int_0^H u^2 \, \mathrm{d}n \tag{12b}$$

$$U\Delta h = \int_0^H ug' \, \mathrm{d}n \tag{12c}$$

$$S_1 \Delta h^2 = 2 \int_0^H g' n \, \mathrm{d}n \tag{12d}$$

$$S_2 \Delta h = \int_0^H g' \, \mathrm{d}n \tag{12e}$$

$$Hw_H - S_3 w_H h = \int_0^H w \, \mathrm{d}n,$$
 (12f)

where S_1 , S_2 and S_3 are shape factors which take on the value of unity for well mixed katabatic flow (Manins and Sawford 1979) and w_H is the entrainment velocity which can be related to the downslope velocity through conservation of mass as:

$$w_H = -\frac{\partial Uh}{\partial s} : ag{13}$$

The latter term can also be simplified using the entrainment coefficient using $E = -w_H/U$.

3 Overview of Valley and Measurement Systems

The LAPSE-RATE campaign was conducted in the San Luis Valley in south central Colorado between 14 and 19 July, 2018. The San Luis Valley (SLV) is a 21,000 km² basin, dimensioned 196 km long by 119 km wide. The SLV is at an average elevation of 2336 m above mean sea level (m.s.l.), and sees significant agricultural use, particularly in the north-western quadrant of the valley. In the north-west corner of the SLV (Fig. 2a), the Saguache mountain valley extends roughly 48 km north-west from the community of Saguache at 2348 m m.s.l., and crosses the U.S. continental divide. These mountains are situated along CO Highway 114, which winds past Houghland Hill, and continues towards the north-west past Lone Tree Gulch at 2590 m m.s.l. and towards North Pass, before descending back towards Gunnison. Moving up the valley to the north-west, slopes on the south-west side of the road are largely eastern-facing, receiving the first insolation from the morning sun. On the north-east side of the road, the mountain ridges are largely aligned along the north-east/south-west axis and



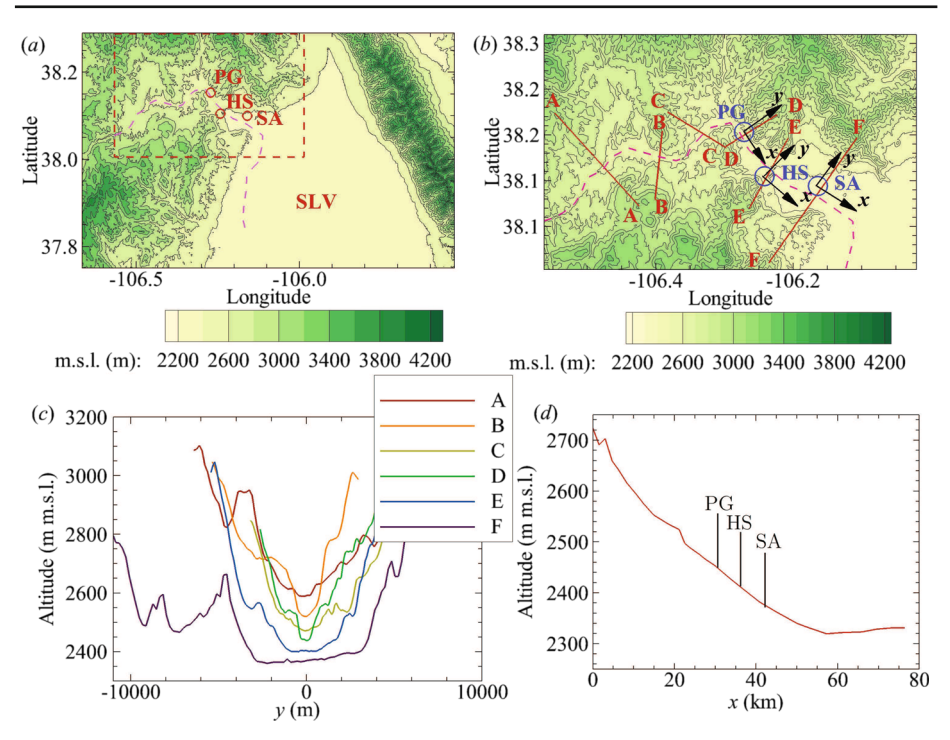


Fig. 2 a Map of the northern half of the San Luis Valley showing Saguache Valley and location of Poison Gulch (PG), Higgins Spring (HS) and Saguache Airport (SA) measurement sites. **b** Detail of Saguache Valley with coordinate system shown as well as lines showing locations of cross-sections of valley shown in (**c**). **d** Height change along pink dotted line in (**a**) and (**b**). Location used for determining (x_R, z_R) , θ_{vR} and s = 0 is the start of dotted line. Local coordinate systems for each measurement location also indicated using arrows

hence the insolation received on this side of the canyon is dependent on the topographic details, with some portions of the canyon walls shaded until after 1100 LT. On the morning of 19 July, twilight initiated at 0519 LT with sunrise at 0550 LT (note that in this manuscript we will use Mountain Daylight time zone (UTC-6) as local time (LT) throughout).

As assessed by the National Cooperative Soil Survey, the surface of the Saguache mountain valley is composed of deep, well-to-somewhat-excessively drained soils formed in mixed alluvium. The surface structure is sandy loam, having moderate to fine granular structure; and composed of 5 percent pebbles producing a gradual, smooth boundary. Vegetation in the valley is composed of native pastureland and irrigated cropland. Native vegetation is mainly needle-and-thread grass, Indian ricegrass, thickspike wheatgrass and four-wing saltbush. These conditions are expected to produce a Davenport roughness length between 0.03 and 0.10 m (Wieringa 1992).

Morning drainage flows into the SLV basin were observed on each day of the LAPSE-RATE campaign (Pinto et al. 2021) and on 19 July LAPSE-RATE measurement assets were deployed to measure them in detail. An overview of the general topography is provided in Fig. 2a. As noted, the focus of this paper is on the drainage flow stemming from the Saguache mountain valley, highlighted in Fig. 2a, and detailed in Fig. 2b–d. The Saguache mountain valley has a relatively shallow slope down to the SLV basin, with average valley bottom incline of $\alpha \approx 0.4^{\circ}$. Ridge tops along either side of the valley (Fig. 2c) have altitudes up to $2800-3100 \,\mathrm{m}$ m.s.l., and sides with angled slopes between 3° and 12° from C to F. Notably



the valley expands from a triangular canyon topography at D to a broader, shallow valley floor at F.

While there were observing platforms positioned throughout the valley of interest, three particular sites are the focus of the current analysis, referred to as Poison Gulch (PG), Higgins Spring (HS) and Saguache Airport (SA) which were located at the locations marked in Fig. 2b, d with the valley cross-sections at these locations corresponding to D, E and F respectively in Fig. 2c. Further information on the observational assets that are not included in the current analysis can be found in (de Boer et al. 2020a, b, 2021b; Pillar-Little et al. 2021; Pinto et al. 2021; Brus et al. 2021; Bell et al. 2021; de Boer et al. 2021a; Islam et al. 2021; Jensen et al. 2021).

For convenience, we define x rotated horizontally such that it aligns with the local mean downslope gradient (a rotation of approximately 150° azimuth). The remaining Cartesian components y and z are defined using the standard right-hand rule with z directed upwards, away from the surface. Slope coordinates are aligned with s along the slope and s normal to the slope as in Fig. 1. However, unless otherwise noted, due to the shallow slopes involved, we assume that locally s0 and s1 such that velocity components s2 is at the surface, such that s3 is referenced above ground level, a.g.l., with the s4 plocation of the origin corresponding the central point of the valley. Note that, since s2 older of the position error associated with this assumption is relatively small over the measurement height, with a vertical difference of less than a centimeter and a horizontal difference of approximately 2 m.

3.1 Poison Gulch

The Poison Gulch (PG) measurement location was located downslope of a change in valley slope direction from northeasterly to southeasterly within a relatively confined portion of the valley. A single DJI M600 multirotor UAS equipped with XQ-2 pressure (P), temperature (T) and relative humidity (RH) sensors (Intermet, Grand Rapids, Michigan, U.S.A.) was operated by the University of Kentucky at this site. Additional detail about this aircraft and sensor systems are available in Bailey et al. (2020) with the calibration and validation results presented in Barbieri et al. (2019).

This aircraft was flown in 700 m long horizontal transects across the valley (approximately corresponding to cross-section D in Fig. 2) with a single flight consisting of transects nominally at 25 m, 50 m, 100 m, 150 m, 200 m and 250 m a.g.l. above the valley floor. Flights were conducted every 30 min from 0530 LT to 1100 LT, with each flight lasting approximately 15 min and samples of P, T and RH collected at a rate of 1 Hz.

3.2 Higgins Spring

Approximately 7 km further to the east, additional observations were collected at the Higgins Spring location. This site, located on the south-western side of the Saguache valley just to the north of County Road CC36 and just west of County Road 42 (south of highway 114) sits at a slightly elevated location from the valley floor, with good visibility to the northern side of the valley. From this location, a fixed-wing X-UAV Talon UAS was operated by the University of Colorado during this event (de Boer et al. 2021b). The relatively small Talon (1.7 m, 3 kg) was configured for an endurance of approximately 45 min, at a cruise speed of 18 m s⁻¹. The Talons operated for LAPSE-RATE carried a RSS904 sensor (Vaisala, Vantaa, Finland), providing measurements of pressure, temperature, and humidity. Wind



magnitude and direction was inferred from the autopilot information using the difference between relative airspeed and ground speed (de Boer et al. 2021b).

For this 19 July case, a Talon was flown in a racetrack pattern stretching across the Saguache Valley, oriented southwest to northeast. These flights approximately spanned leg E in Fig. 2. Conducting six total flights on this morning, these racetracks were flown at a variety of stepped altitudes ranging between 30 and 350 m a.g.l., with altitudes generally increased at 50 m intervals. It is important to note that the aircraft altitudes are relative to the takeoff altitude, and therefore the sampling was higher over the Saguache River, in the lowest part of the valley. These flights began at 0615 LT.

3.3 Saguache Airport

The Saguache Airport (SA) measurement location was at the Saguache Municipal Airport (04V). This site was situated at a broad portion of the Saguache mountain valley prior to where the valley exited into the SLV basin. In addition to the data from five UAS platforms operated by the University of Kentucky (three fixed-wing and two multirotors) at this location, the SA site measurements also included an airport automated weather observing system (AWOS), providing ground-level P, T, RH, wind, cloud height and precipitation at 20 min intervals, and a Doppler lidar system. This wind-measuring lidar system was a Leosphere WindCUBE v1 (Vaisala, Vantaa, Finland) system operated by the University of Colorado, as described in Sanchez Gomez et al. (2021) and Bell et al. (2021). The lidar was collocated with the AWOS system and was measuring 2 min averages of the vertical profiles wind speed and direction at 20 m intervals from 40 m to 200 m a.g.l..

All UAS and their instrumentation operated at this site are described in detail in Bailey et al. (2020) with the validation of their measurement systems against a common, groundbased standard provided in Barbieri et al. (2019) so only a brief description is provided here. Three fixed-wing UAS, of a type referred to as BLUECAT 5 and based on the Skywalker X8 platform were flown from the south-eastern end of the Saguache Airport runway, approximately corresponding to leg F in Fig. 2. These aircraft measured wind velocity and direction using a custom five-hole probe, as well as P, T and RH using an XQ sensor (Intermet, Grand Rapids, Michigan, U.S.A.). As detailed in Bailey et al. (2020), samples from each measurement system were upsampled through interpolation to 200 Hz, to match the rate at which position information was acquired, although sensor response rates were much lower (1 Hz for P, T, and RH and 30 Hz for the three wind components. Two fixed-wing aircraft measured nominally 1700 m long transects across the valley at 100 m a.g.l. and 150 m a.g.l., with the third flying transects at 200 m a.g.l. and 400 m a.g.l.. Note that the valley floor at this location in the valley had a $\sim 0.5^{\circ}$ transverse (cross-valley) slope (Fig. 2c), so the horizontal transects were designed to maintain near-constant height a.g.l. These flights were conducted from 0700 to 1100 LT with intermittent breaks to change batteries and relaunch the aircraft.

A multirotor UAS based on the 3DR SOLO platform also conducted vertical profiling measurements at the same site. The aircraft was equipped with an XQ-2 sensor for measuring *P*, *T* and *RH* and a sonic anemometer (Trisonica Mini, Anemoment, Longmont, Colorado, U.S.A.) to measure wind speed and direction. This UAS conducted near-continuous vertical profile measurements from 10 to 100 m from 0530 to 1100 LT. For this aircraft, samples from each measurement system were re-sampled through interpolation to 10 Hz, to match the rate at which position information was acquired.

A second multirotor UAS based on the DJI S1000 platform was also used for vertical profiling. This UAS was equipped with XQ-2 sensors for measuring P, T and RH and a



sonic anemometer (81000, R.M. Young, Traverse City, Michigan, U.S.A.) to measure wind speed and direction. This UAS conducted hourly vertical profile measurements from 10 to 300 m from 0600 to 1100 LT. Note that the sonic anemometer measurements from this aircraft were not included in this analysis as the lidar data provided higher temporal resolution over a similar altitude range for the observation period.

3.4 General Weather Conditions

A high pressure region developed over Colorado on 17 July which was still established on the measurement morning of 19 July. Data from the AWOS station and lidar located at Saguache Airport (Fig. 3) show that this period brought a consistent diurnal cycle in temperature (15 to 20 °C), with early morning temperatures around 10 to 15 °C and afternoon temperatures exceeding 30 °C. The early morning hours of 19 July saw thin high cloud cover, which limited the extent of radiative cooling overnight. However, significant cooling still occurred, with temperatures at the SA site dropping to 13 °C overnight. This drop in temperature corresponded to an increase in relative humidity to 60%. As the morning progressed, the sun heated the terrain in the valley, and in particular east- and south-facing slopes, resulting in the development of buoyancy-driven convection, vertical motion over the mountain sides, and the reversal of the drainage flow to an up-valley wind regime at approximately 0800 LT. Surface winds were relatively weak during the UAS observation period, at approximately 2 m s⁻¹. Observations from the lidar during the UAS observation period will be discussed in greater detail later, but show slightly higher wind magnitude above 40 m a.g.l. reaching 7 m s⁻¹, with the winds reversing direction between 0800 and 0900 LT.

4 Observations and Discussion

4.1 One-Dimensional Assessment

We first examine the katabatic flow within the context of the one-dimensional approximation presented in Sect. 1. To investigate the evolution of the one-dimensional parameters, the integral quantities were calculated from the time-averaged vertical profiles of u and θ_v for each UAS flight following 12. Note that, to do so, the average winds above the layer were first subtracted from u and the assumption $z \approx n$ applied before integrating using 12a, b to obtain Uh and U^2h . The ambient lapse rate, γ , was first determined using the linear portion of the measured θ_v profile. This lapse rate was then subtracted from θ_v to determine δ . Reference θ_{vR} values were approximated from the ambient lapse rate outside the katabatic layer using the estimated α and distance from assumed initiation point, as indicated on Fig. 2. The resulting δ profiles were then transformed to g' profiles following 6a and integrated as in 12c, d, e assuming $z \approx n$ to obtain corresponding values of $U \Delta h$, $S_1 \Delta h^2$ and $S_2 \Delta h$. As wind information was not available from the PG measurements, only the latter two terms could be obtained for this location. Furthermore, due to the presence of non-uniform wind velocity above the katabatic and anabatic layer, there was some ambiguity in the integral upperbound (for which we use the estimated layer height, H) when integrating the wind profiles, and hence the magnitude of wind above the layer. Thus, the calculation was conducted both assuming H was located at the local minimum of u and assuming H was at the upper bound of the measurement. Note that this ambiguity in H was less important for the g' profiles as $g'(z) \to 0$ as z increases.



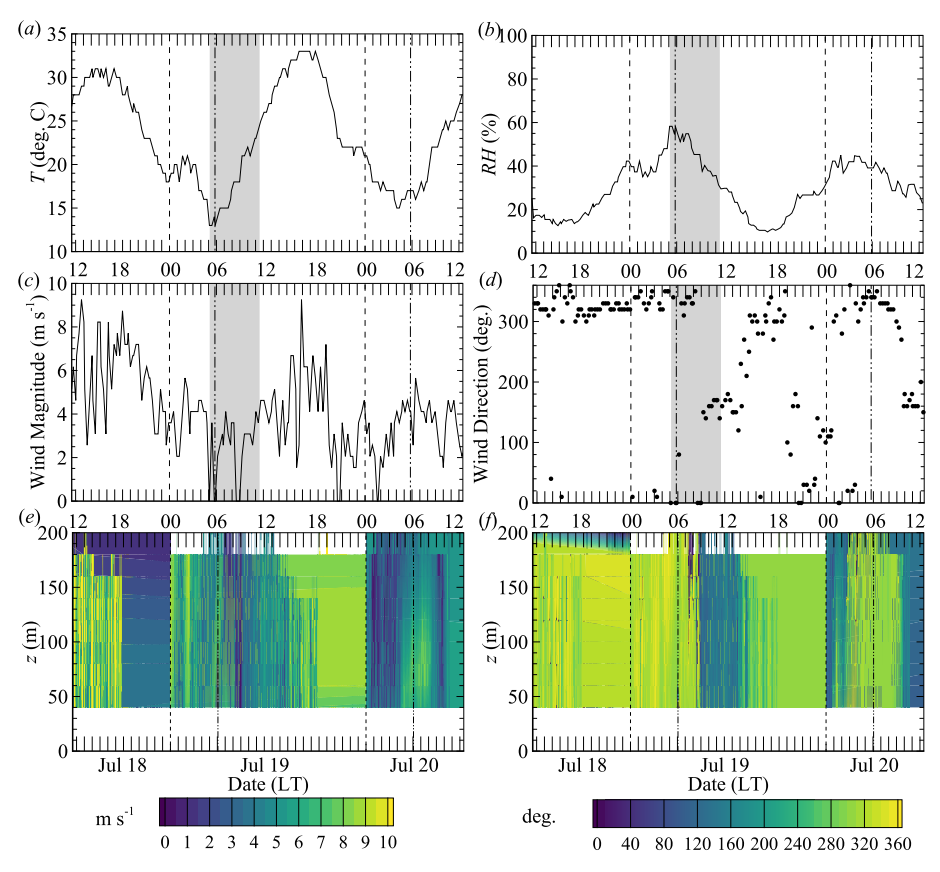


Fig. 3 Surface observations from Saguache Airport AWOS station showing: **a** temperature at 2 m a.g.l.; **b** relative humidity at 2 m a.g.l.; **c** horizontal wind magnitude; and **d** direction at 10 m a.g.l.. Also shown are lidar observations of **e** horizontal wind magnitude and **f** direction. Grey region indicates UAS observation period on the morning of 19 July, dashed line indicates local midnight, dash-dot-dot line indicates sunrise

The resulting time-dependence of Uh, U^2h , $U\Delta h$, $S_2\Delta h$ and $S_1\Delta h^2$ for each site is shown in Fig. 4. Where multiple estimates were available for the same quantity, (i.e. by changing the limits of integration) the average value was then calculated from the different estimates and the standard deviation is treated as the uncertainty of the corresponding value.

The quantities shown in Fig. 4 were then used to estimate the corresponding time dependence of one-dimensional velocity U, buoyant forcing Δ and layer height h. For example, at the HS and PG sites, the layer height could be found from $h = (Uh)^2/(U^2h)$, allowing the streamwise momentum to be found from U = (Uh)/h and buoyant forcing from $\Delta = (U\Delta h)/(Uh)$. A second estimate of U and U could also be found from calculating U from $U = U^2h/(Uh)$ and then using this value to find U = (Uh)/U. To find $U = U^2h/U$ at the PG site, an alternate approach was required whereby constant shape factor values $U = U^2h/U$ and $U = U^2h/U$ were assumed such that an estimate of layer thickness $U = U^2h/U$ could be found from U = (Uh)/U allowing the buoyant forcing $U = U^2h/U$ to be found from U = (Uh)/U and $U = U^2h/U$ allow consistent comparison between sites, this calculation of $U = U^2h/U$ and $U = U^2h/U$ and $U = U^2h/U$ and $U = U^2h/U$ and $U = U^2h/U$ allow consistent comparison between sites, this calculation of $U = U^2h/U$ and $U = U^2h/U$



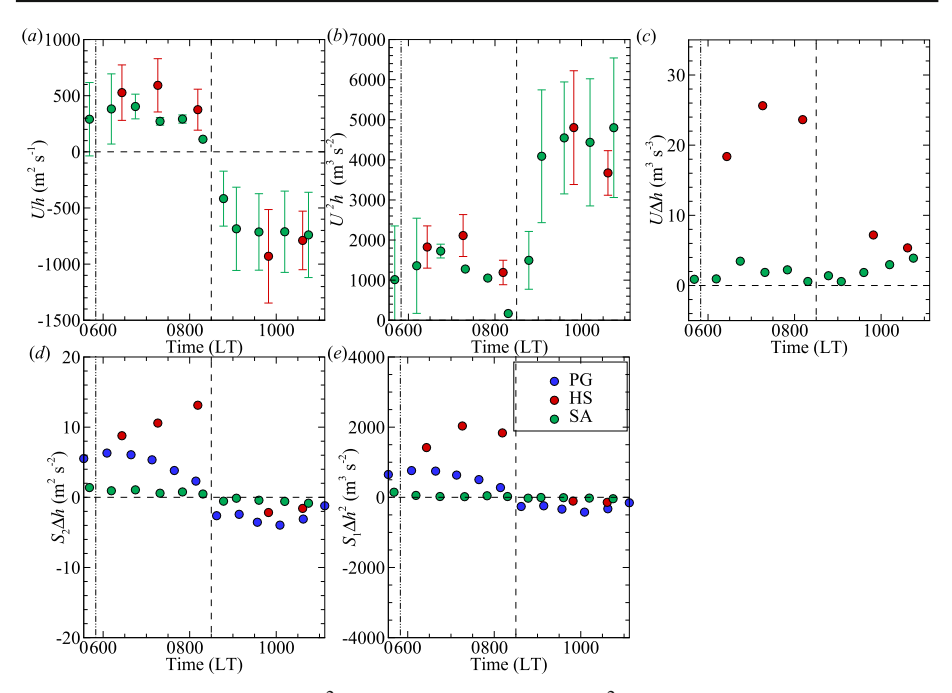


Fig. 4 Integral quantities: $\mathbf{a}\ Uh$; $\mathbf{b}\ U^2h$; $\mathbf{c}\ U\Delta h$; $\mathbf{d}\ S_2\Delta h$; and $\mathbf{e}\ S_1\Delta h^2$. Horizontal dashed line indicates zero level, vertical dashed line indicates approximate time of transition from katabatic to anabatic flow. Error bars indicate standard deviation where multiple estimates were available for the same quantity. Vertical dash-dot-dot line indicates sunrise

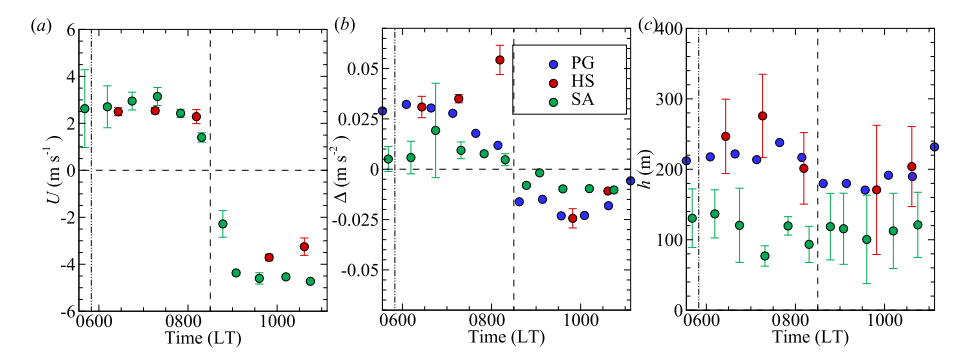


Fig. 5 Characteristic scales: $\mathbf{a}\ U$; $\mathbf{b}\ \Delta$; and $\mathbf{c}\ h$. Horizontal dashed line indicates zero level, vertical dashed line indicates approximate time of transition from katabatic to anabatic flow. Error bars indicate standard deviation where multiple estimates were available for the same quantity. Vertical dash-dot-dot line indicates sunrise

sented with the standard deviation treated as the uncertainty in the corresponding value. The resulting time evolution of U, Δ and h are presented in Fig. 5.

Focusing first on the temporal behavior of momentum per unit width, Uh, Fig. 4a shows that the katabatic flow momentum peaks at approximately 0715 LT at the HS site, but remains relatively constant at the SA site. Figure 4a also shows that the flow transitions to being anabatic at the SA site at approximately 0830 LT. Although there was not enough temporal resolution to identify the time of transition at the HS site, the hydrostatic and buoyant forcing



for the PG site (Fig. 4d, e) appear to transition at approximately the same time, suggesting that the flow reversed throughout the valley simultaneously.

Importantly, Fig. 4a indicates that katabatic flow momentum is lost between HS and SA locations during katabatic flow. As revealed in Fig. 5a, c, this manifests in reduced depth of the layer, with U remaining nearly constant at approx 3 m s⁻¹ at both locations. This thinning of the katabatic layer is counter to that expected by analytical solutions of the one-dimensional equations (e.g. Princevac et al. 2008), which suggest h will increase along the slope due to the buoyant and hydrostatic forcing and the additional momentum added by side-slope flow (e.g Sato and Kondo 1988). Note that a rough volumetric flow rate analysis confirms that the reduction in h between HS and SA cannot be attributed to the increased width of the valley between the two sites, as even accounting for this change in width (from approximately 4 km to 6 km), the momentum is still approximately halved (due to h dropping from \sim 200 m to \sim 100 m while U remains unchanged).

Noting that since U is approximately constant during the katabatic flow period, we can recast the local and advective acceleration in 9 as:

$$U\frac{\partial h}{\partial t} + U^2 \frac{\partial h}{\partial s} : . {14}$$

As both positive and negative $\partial h/\partial t$ rates were observed, this suggests that the negative $\partial h/\partial s$ can be attributed to the balance of forcing terms in 9. However, Fig. 4d, e show that during the katabatic flow period both $S_2\Delta h$ and $-\partial/\partial s(S_1\Delta h^2)$ remain positive, indicating that both the hydrostatic pressure and buoyant forcing will be adding to the momentum of the flow and not decreasing it. Hence, the one-dimensional approximation of the katabatic flow would suggest that the turbulent skin friction and turbulent momentum transport out of the layer are responsible for its thinning as it evolves downslope. Although these processes are likely to at least partly responsible for the loss of momentum, as will be shown in the following section, more detailed examination of the temporal and spatial behavior of the flow suggests the thinning of the layer can be attributed to three-dimensionalities which reduce the validity of the one-dimensional approach in this particular case.

Further details about the evolution of the flow between the sites can be extracted from the profiles of g' and u. The time-averaged vertical profiles of g' calculated for each flight are presented in Fig. 6a–c for the katabatic flow period (before 0830 LT) and in Fig. 6d–f for the anabatic flow period (after 0830 LT). At the PG site, Δ appears to well represent the katabatic flow, as indicated by Fig. 6a, d through the collapse of the g' profiles normalized by Δ and h. However, the form of the scaled profiles changes significantly between katabatic and anabatic flow, with the downslope-forced profiles having a maximum value at z/h = 0.25. Conversely, the maximum for the upslope-forced profiles occurring just above the surface, indicating that the upslope forcing arose from more local surface warming.

Similar collapse of the profiles was also observed at the HS site, shown in Fig. 6b, e. Notably, the shape of the profiles is slightly different than that observed at the PG site during the katabatic period, with a less prominent peak within the layer. Note also that increased scatter was observed in profiles measured close to the transition from katabatic to anabatic flow as g' became weaker, with variability within the uncertainty of the instruments. At the furthest downstream site, SA, even more variability is observed in the normalized profiles, shown in Fig. 6c, f. To some extent this represents the uncertainty in h and Δ , which will be shown later to be introduced by the time scales of the key features of the katabatic flow being faster than the UAS's ability to measure the profile. Despite this uncertainty, the profiles of $g'/|\Delta|$ during the katabatic period appear similar to those presented in Fig. 6a, but are much



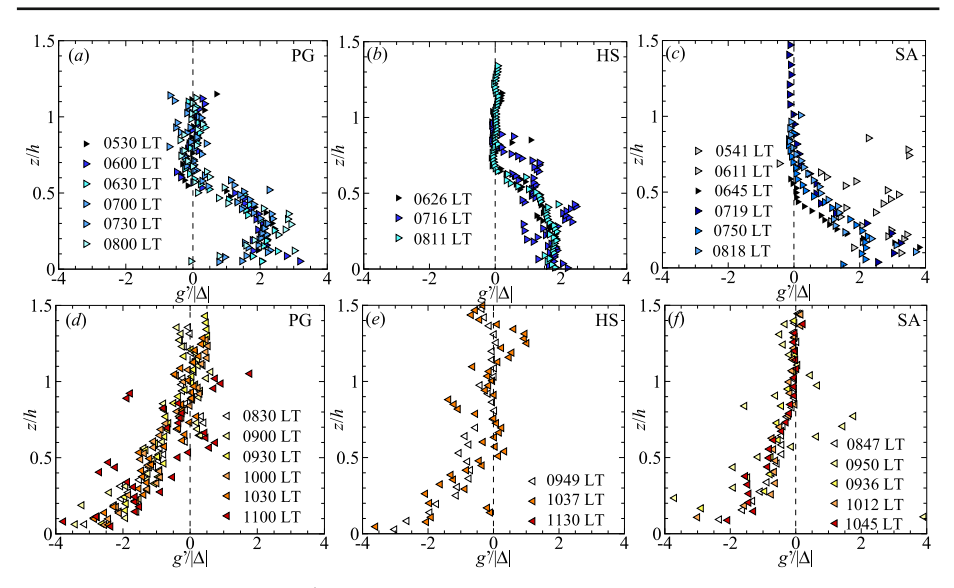


Fig. 6 Time-averaged profiles of g' shown normalized by $|\Delta|$ for katabatic flow period at: **a** PG; **b** HS; and **c** SA sites. Corresponding profiles for anabatic flow period shown in (**d**-**f**). Different colored symbols represent different profiles measured at different times in the morning

less full with the reduced gravity more concentrated in the lower portion of the layer with an apparent peak in the profile near z/h = 0.1.

Corresponding time-averaged profiles of the downslope velocity are shown in Fig. 7 for the HS and SA sites. There is significantly different behavior at both sites during the katabatic flow period (Fig. 7a, b), potentially due to the presence of non-zero velocity above the katabatic layer. Note that similar streamwise dependence of flow profiles was also observed by Pinto et al. (2006) who attributed this behavior to intermittent interactions between the low-level and elevated winds through vertical mixing events. At the HS site, the katabatic jet is only slightly faster than the flow above the katabatic layer, peaking at u/|U| = 3 at z/h = 0.5. At the SA site, the out of layer flow is weaker, resulting in a lower peak at z/h = 0.25, reaching u/|U| = 2. The measured profiles from the anabatic flow period were quite similar for both sites and reflect the characteristics of a well-mixed boundary layer.

As noted, increasingly more scatter was observed in the katabatic flow profiles of both $g'/|\Delta|$ and u/|U|, as the flow traveled downstream from PG to HS to SA. This scatter is a result of the increased unsteadiness, particularly observed at the SA site when compared to the PG site. This unsteadiness takes the form of low frequency pulsations. These pulsations are illustrated in time-dependent U, Δ and h calculated using vertical profiles taken roughly 90 s apart, and shown in Fig. 8. Note that to better highlight the periodicity, these results are presented with a 9-min rolling average. During the katabatic flow period, it is shown that both positive and negative instances of Δ occur at this site, with the maximum value of 0.03 observed at 0700 LT similar to that observed at the HS and PG sites for the same time period. The reversal of anabatic forcing, in the form of consistently negative Δ , also becomes less evident, with positive Δ observed well after U switches to the upslope direction. The details of the katabatic flow time-dependence are further explored in the next section.



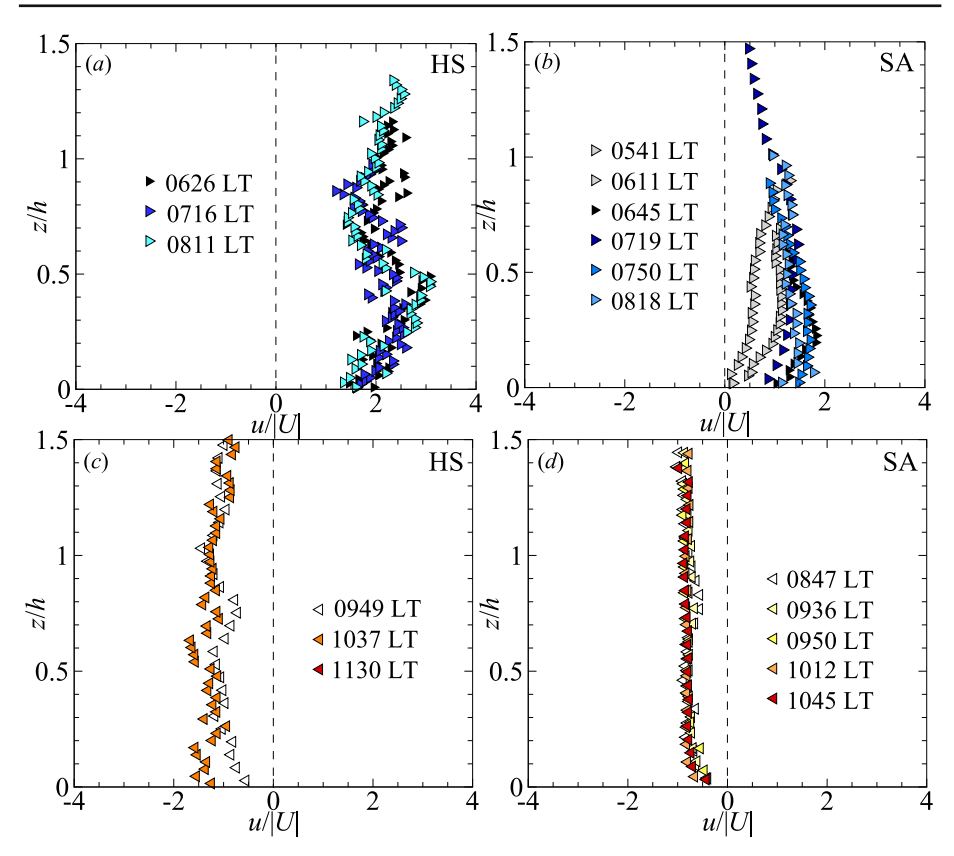


Fig. 7 Time-averaged profiles of u shown normalized by |U| for katabatic flow period at: **a** HS; and **b** SA sites. Corresponding profiles for anabatic flow period shown in (**c**) and (**d**). Different colored symbols represent different profiles measured at different times in the morning

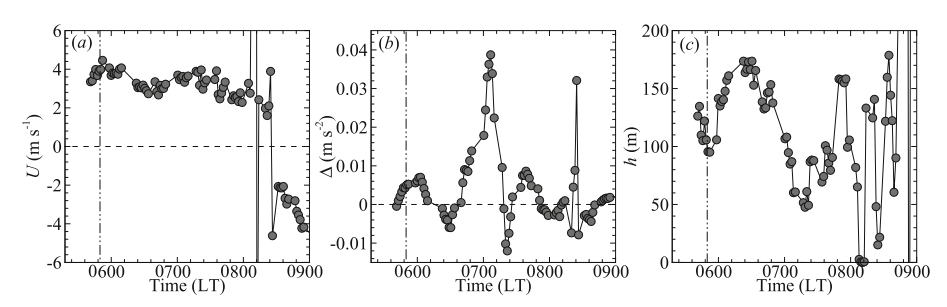


Fig. 8 Characteristic scales: $\mathbf{a}\ U$; $\mathbf{b}\ \Delta$; and $\mathbf{c}\ h$ calculated at SA site using profiles measured every two minutes. Horizontal dashed line indicates zero level. Vertical dash-dot-dot line indicates sunrise

4.2 Temporal and Three-Dimensional Details of the Katabatic Flow

An overview of the temporal dependence of the katabatic flow within the confined canyon at the PG site is provided in Fig. 9a in the form of a time-height plot of θ_v , where θ_v has been averaged at constant z across the canyon. Figure 9a illustrates that the stable layer persisted



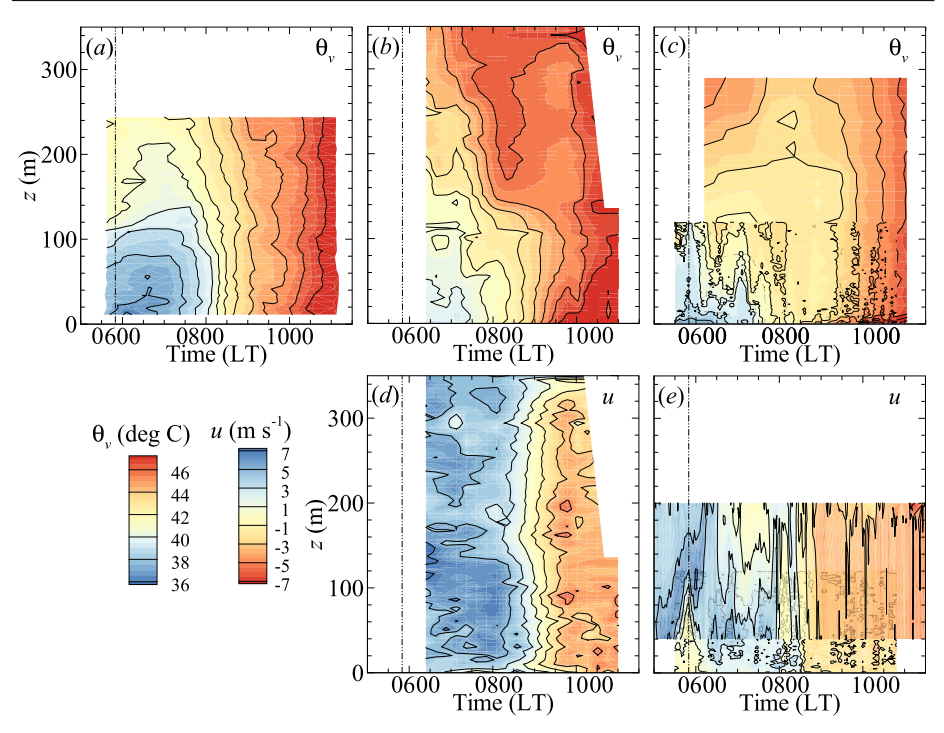


Fig. 9 Time-height plots of θ_v measured at **a** PG site; **b** HS site; and **c** SA site. Corresponding time-height plots of u also shown for **d** HS site and **e** SA site. Contours in **c** show temperatures measured from both S1000 for z > 100 m and SOLO UAS for z < 100 m. Contours in **e** show Doppler lidar values for z > 40 m and values from the SOLO UAS for z < 40 m. Vertical dash-dot-dot line indicates sunrise

near the surface until approximately 0830 LT, forming an inversion above 100 m which lasts until 0900 LT and developing into a near-surface super-adiabatic layer by 1000 LT. At 0700 LT the stable layer appears to thicken briefly, before receding to the previous thickness. However, the θ_v behavior during the katabatic flow period was generally steady.

Further downslope, at the HS site, increased unsteadiness in θ_v was observed over the same period, with generally warmer temperatures measured, as shown in Fig. 9b. The unsteadiness is also evident in a brief incursion of warmer air above z=150 m at 0800 LT which was not evident at the PG site. As the canyon flow expanded into the wider valley encompassing the SA site, the katabatic flow behavior became even more unsteady, as presented as time-height dependence of θ_v shown in Fig. 9c. At this location, the θ_v dependence suggests that, in general, the colder air flow persisted until approximately 0730 LT, with an inversion of temperature forming near the surface evident after approximately 0830 LT. However, the inversion is less distinct than observed at the HS site. Furthermore, the time-dependence shows that the colder air had an increasingly pulsatile nature, with a period of about 30 min, as the canyon drainage flow expanded into the valley.

The corresponding time-height dependence of the down-valley component of wind, u, is shown in Fig. 9d from the UAS measurements at the HS site and in a composite of the lidar and UAS results at the SA site in Fig. 9e. These figures show that, while the HS site had largely uniform katabatic and anabatic winds (as previously observed in the discussion of Fig. 7), the SA site had significant temporal variability in the katabatic winds. Most significantly, it can



be observed that the downslope flow detached from the surface between 0500 LT and 0630 LT at the SA site, resulting in the presence of stagnant air near the surface and a brief period of non-canonical katabatic flow more akin to a low-level jet. Once the flow transitioned to becoming up-slope flow, it became much more uniform and similar to that observed at the HS site.

The period of oscillations observed in Fig. 9c, e at the SA site is also reflected in Fig. 8b, where it can also be observed that the period changes in time. In both, the period was initially ~ 60 min, but decreased to ~ 30 min towards the end of the katabatic flow period.

This oscillation period is larger than the period that could be expected for gravity waves. In addition, internal-wave oscillations associated with the Brunt-Väisälä frequency (Van Gorsel et al. 2003), here $N = (g\gamma/\theta_{vR})^{1/2} = 0.0245$ for the katabatic flow, would correspond to a period of ~ 250 s. Turbulence time scales would be even smaller, on the order of the surface shear $0.25h/U \sim 15$ s. Note that Princevac et al. (2008) suggest that longer period oscillations can be produced by critical internal waves with period of $2\pi/(N \sin \alpha)$ but the shallow slope in the present case would result in these waves having periods on the order of 10 h. An alternative mechanism capable of introducing periodicity (Fleagle 1950; McNider 1982; Helmis and Papadopoulos 1996; Van Gorsel et al. 2003) can be through adiabatic heating due to friction and radiational cooling, and is expected to produce oscillations with a period of $2\pi\theta_{vR}^{1/2}/(g\gamma\sin^2\alpha)^{1/2}$ which would be ~ 25 min for this case. Additional time scales on the order of 10 to 70 min can also be introduced by tributary flows entering the main valley (Porch et al. 1991) or variation of cold air sources upstream (Allwine et al. 1992) which are also consistent with the period of the oscillations observed at the SA site. Observations of Kelvin-Helmholtz waves have also been made in drainage flows (e.g. Pinto et al. 2006, who observed waves with periods of 5 min to 20 min).

Importantly, however, Fig. 9a indicates the unsteadiness evident at the SA site was not present in the more confined canyon at the PG site, suggesting that the instability is introduced as the flow expands into the shallower valley towards the HG and SA sites. This suggests that the unsteadiness could be introduced by Kelvin–Helmholtz-type waves along the *y*-axis if the flow issuing from the canyon does not fill the valley. Such waves would be expected to have a wavelength on the order of the canyon width at the location where the katabatic flow separates from the side walls of the valley. For the present case this would result in wavelengths on the order of 4km to 8km. The resulting period would be on the order of 30 min, assuming a downslope flow velocity of 3 m s⁻¹.

Evidence in support of the presence of horizontal Kelvin–Helmholtz waves is presented in Fig. 10, which shows time-span plots produced from the fixed-wing UAS measurements of θ_v and u across the SA site at z=100 m and z=150 m. Significant horizontal gradients and asymmetry in θ_v were measured across the SA site. The colder air was concentrated to the south-western portion of the valley (negative y) where slightly lower elevations were present (Fig. 2).

Correlation between the temporal dependence of the katabatic wind and θ_v with that of the vertical profiles of Fig. 9c, e is evident, with katabatic winds measured until 0830 LT at the z=100 m but receding earlier at z=150 m, reflecting a thinning of the drainage flow. At z=100 m the winds were consistently down-valley for y<0 m, but were intermittently down-valley, up-valley and calm for y>0 m during the drainage event. After 0830 LT, when anabatic flow formed, the horizontal gradients in θ_v and u dissipated.

The concentration of the cooler air and downslope winds to the south-western side of the valley indicates that the flow did not fill the valley uniformly. Furthermore, these measurements indicate that the drainage flow became increasingly narrow over the course of



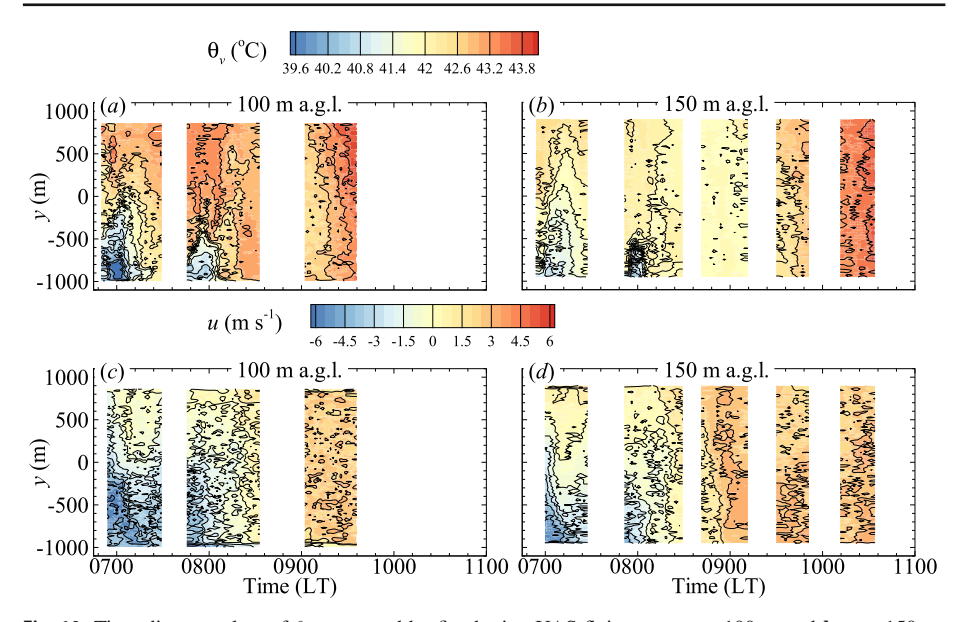


Fig. 10 Time-distance plots of θ_v measured by fixed-wing UAS flying at ${\bf a}\ z=100$ m and ${\bf b}\ z=150$ m. Corresponding measured downslope wind component shown in ${\bf c}$ for z=100 m and ${\bf d}$ for z=150 m. Gaps in contours indicate periods between measurement flights

the morning. More relevant to the above discussion, is the presence of spanwise periodicity in both the θ_v and u measurements, initially having a period of 30 min but decreasing to 15 min as the width of katabatic flow decreased prior to the initiation of uniform up-slope flow. Notably, the vertical profiling location near y=0 appears to be at the northern edge of the katabatic flow, despite being centrally located in the valley. Hence, the influence of spanwise instabilities on the vertical profiles was likely increased. However, Fig. 10 shows that the spanwise unsteadiness was significant across the measurement range

Insight as to why the asymmetry occurred at the SA site can be extracted from the y-dependence of flow features at the PG and HS sites. The θ_v y-dependence at the PG site is presented in Fig. 11. Not only do the θ_v contours show strong z-dependence until flow reversal (Fig. 11a–f), but significant y-direction asymmetry across the valley can also be observed, with colder air at the east-facing (negative y) side of the valley for z < 150 m and at the west-facing (positive y) side of the valley for z > 150 m.

Similar behavior is also evident in the spanwise θ_v distribution measured at the HS site, shown in Fig. 12a. Similar accumulation of colder air was measured in the north-facing side of the valley prior to transition to up-slope flow. Also, consistent with the 0730 LT measurement from the PG site, during the 0800 LT measurement at the HS site, stronger horizontal gradients were observed above z=200 m, with colder air observed towards the south-facing side of the valley.

Evidence of accumulation of the katabatic flow towards the south-western portion of the valley is corroborated by the contours of u, shown in Fig. 12b. These observations show asymmetry in u during the katabatic flow period, with the fastest downslope flow observed along the north-facing slope of the valley, near y = 0 and generally slower velocities measured along the west-facing slope.



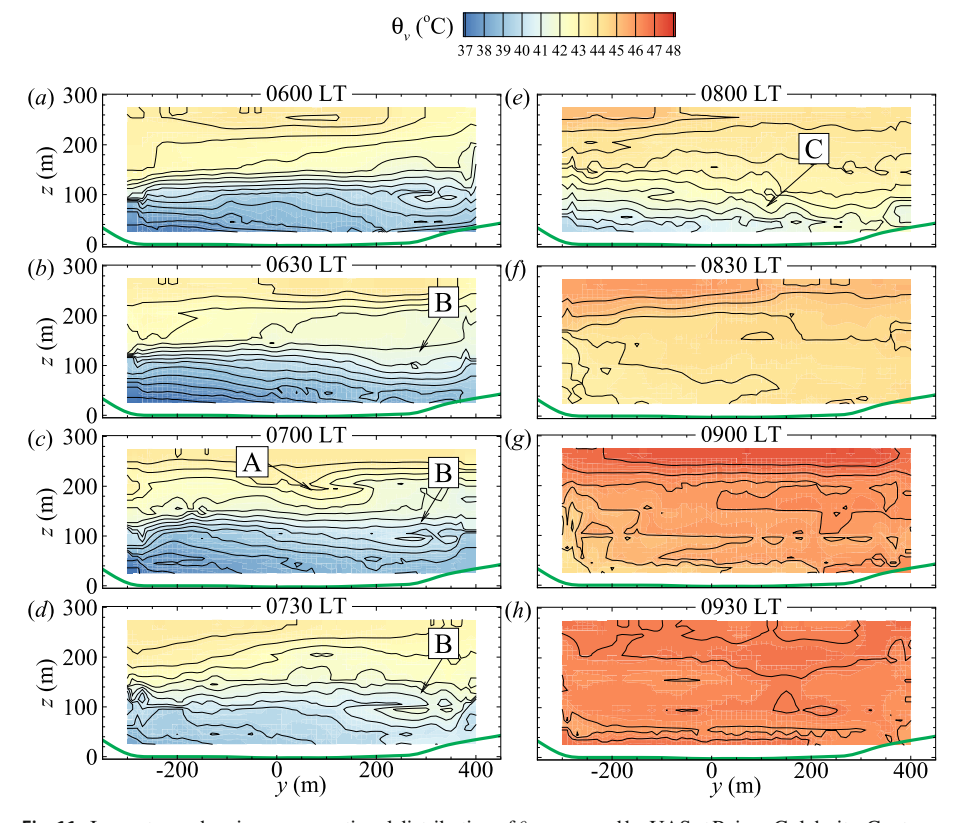


Fig. 11 Isocontours showing cross-sectional distribution of θ_v measured by UAS at Poison Gulch site. Contours are shown from a perspective looking up-valley with y=0, z=0 the initial takeoff point of the UAS. Green line indicates the approximate surface elevation in this coordinate system. Times are ± 15 min due to time required to execute measurement

The PG site θ_v measurements shown in Fig. 11 also reveal the signatures of waves and rolls throughout the morning (e.g. as indicated by A, B, C in Fig. 11), most notably in the upper portion of the measurement region. The asymmetry and evidence of waves in the cross-sections of θ_v suggest the presence of cross-sectional currents, with examination of the time dependence suggesting a relatively slow clockwise rotation.

Supporting the suggestion of cross-sectional currents is evidence of spanwise waves and rolls at z = 200 m, particularly in Fig. 11c (indicated by A), and the entrainment of warmer air towards the surface at z = 100 m on the west-facing (positive y) side of the PG measurement site (indicated by B).

Evidence of cross-section currents is also found in the HS site observations. Estimates of v and w (Fig. 12c, d) at 0630 LT show positive v near the surface and negative v above $z=200\,\mathrm{m}$ coupled with generally negative w for y<500 and positive w for y>500, reflecting a large-scale circulation through the valley. The circulation appears to have weakened by 0715 LT, but evidence of its presence is still discernible. At 0800 LT, the cross-sectional currents reverse, with negative v near the surface and positive v above $z=200\,\mathrm{m}$, although no clear trend in w, and hence no large-scale rotation, is evident. Once transition to up-slope flow has occurred, the cross-sectional currents, although still evident, are greatly weakened.



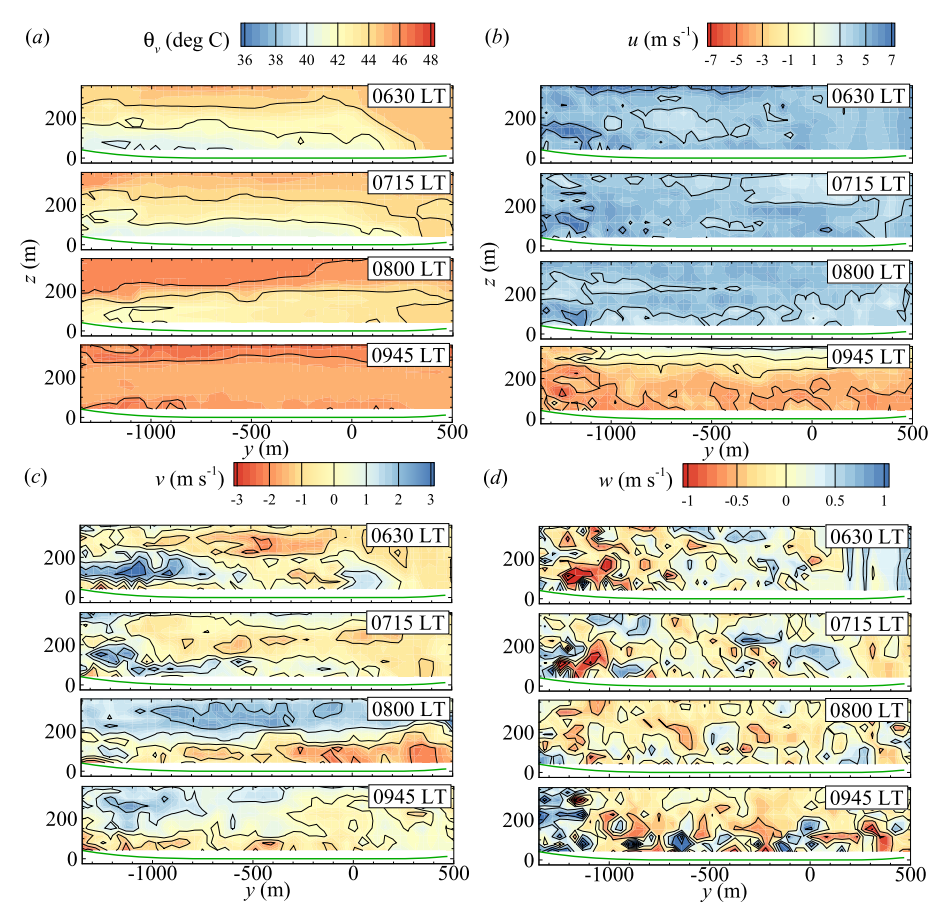


Fig. 12 Isocontours of a θ_v ; b u; c v; and d w estimated by fixed-wing UAS flying across valley at HS site. positive w is in positive z direction

Although differential heating, for example due to shadowing by the valley sidewalls or heterogeneous soil composition, could contribute to the spanwsise density gradients, we hypothesize that the concentration of katabatic flow towards the east-facing wall at both the PG and HS sites can be attributed to the approximately 90° bend in the canyon upslope of the PG site (see Fig. 2). By forcing the katabatic flow to turn, the canyon walls introduce a positive $\partial P/\partial y$ gradient (where positive y is aligned away from the canyon wall innermost to the turn) that will accelerate the stratified flow in the negative y direction and concentrate the katabatic flow towards the east-facing canyon wall. The net result would be the observed coalescence of dense air towards the east-facing (negative y) portion of the valley. This asymmetry persisted in the katabatic flow as it expanded towards the SA site.

The circulation in the valley can also be attributed to the bend upstream of the PG site. The process described above will also introduce *z*-aligned vorticity in the flow. Downstream of the bend, this component of vorticity will rotate to align with the *x*-direction due to vorticity twisting (or tilting) introduced by the vertical shear in the katabatic flow. This effect will be amplified or damped by the balance of baroclinic forcing introduced by the spanwise density gradients, geostrophic winds, and asymmetry in the katabatic flow down the canyon



side walls. The reversal of cross-flow observed at the HS site at 0800 LT is then likely to be introduced through asymmetric radiative heating of the canyon sidewalls.

The net result is heterogeneity in the katabatic flow which contradicts the assumptions within the one-dimensional model of 9 to 13 that is introduced upstream of the SA site, whose broad and flat geometry should be amenable to such assumptions. More importantly, the asymmetry was not captured by the high-resolution numerical simulations used for operational forecasting and assimilation studies for LAPSE-RATE (Pinto et al. 2021; Jensen et al. 2021). This reflects on the importance of unresolved topography and associated processes on grid-scale dynamics.

5 Summary

An early morning katabatic flow emerging from a narrow canyon into a broad valley was studied using uncrewed aircraft systems (UASs) as part of the Lower Atmosphere Profiling Studies at Elevation a Remotely-piloted Aircraft Team Experiment (LAPSE-RATE) campaign. Of particular interest was the effect of the complex inlet topography on the evolution of the flow into the shallower valley around the Saguache Airport measurement location.

Fairly weak katabatic flows were observed during the observation period, likely due to limited radiational cooling in the presence of a high thin clouds that were present overnight. However, the UAS measurements allowed determination of characteristic thickness, h, and characteristic buoyancy deficit, Δ , at three sites, with characteristic velocity, U, able to be determined at two sites. These quantities were found to reasonably scale the measured downslope velocity and reduced gravity profiles at each site, although different scaled Δ profiles were measured within the upstream canyon than within the shallower valley downstream. Furthermore, the broader, nominally-two-dimensional valley was found to contain more scatter in the profiles due to low-frequency motions with period of ~ 15 to 60 min.

This periodicity was consistent with wavelengths which would be expected due to Kelvin–Helmholtz-type waves introduced by spanwise velocity gradients. Evidence of such waves coincided with observations of inhomogeneity in the spanwise direction, which also corresponded to a concentration of the drainage flow towards the south-western side of the valley.

The inhomogeneity and unsteadiness of the observed flow features are summarized in Fig. 13. As illustrated in the figure, the source of the asymmetry in the drainage flow was attributed to the presence of a 90 degree curve in the canyon prior to expansion into the broader valley. This bend is expected to introduce horizontal pressure gradients as the drainage flow traverses the bend, as well as vertically-aligned vorticity due to the resulting spanwise velocity shear. This vorticity would then be reoriented into the streamwise direction by the vertical shear of velocity through vortex twisting compounded with baroclinic forcing. The rotation and concentration of flow towards the south-western portion of the valley persists downstream and couples with the formation of Kelvin–Helmholtz waves introduced as the katabatic flow expands out of the canyon into the broader portion of the valley. Note that these waves were also observed in the data from ground-vehicle-born meteorological sensors traversing along roadways near the exit of the Saguache Valley (de Boer et al. 2021c).

Such rotation, waves and spanwise velocity gradients are not captured in the the onedimensional integral form of the governing equations which assume homogeneity in the spanwise direction. In this case, despite the boundary conditions being suitable for the assumption of homogeneity at the measurment location furthest downstream, the asym-



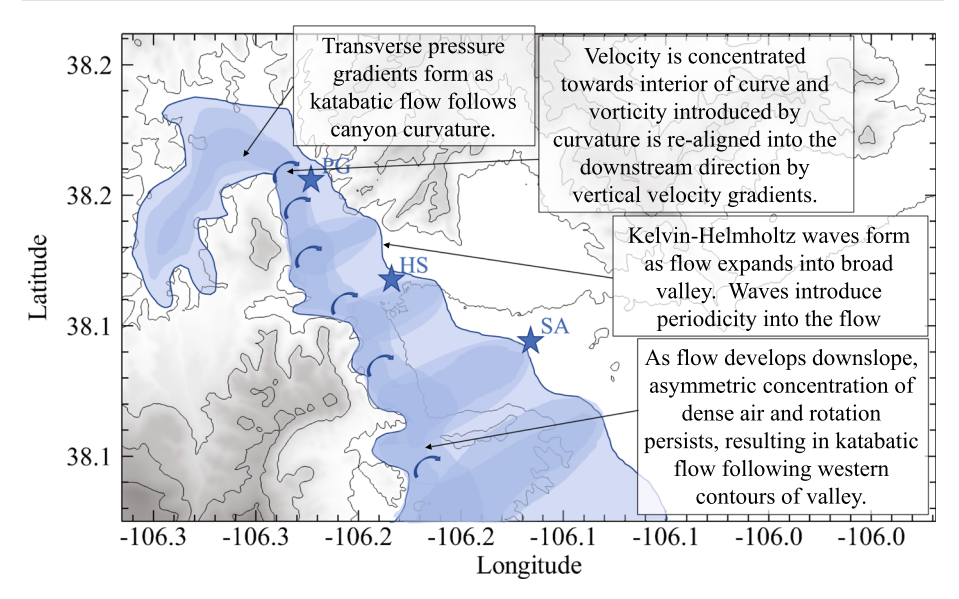


Fig. 13 Sketch of katabatic flow features inferred from observations

metry and secondary motions within the primary katabatic flow at the inlet of the broader portion of the valley resulted in the katabatic layer not thickening along the valley centerline as predicted by the integral form of the equations of motion. These observations reflect the importance of initial conditions on the evolution of downstream flow and the limitations of idealized models in capturing complex flow physics intrinsic to flows in natural terrain.

Data Availability The datasets generated during LAPSE-RATE and analysed in the current study are available from the Zenodo.org data repository (DOI: 10.5281/zenodo.4096451; 10.5281/zenodo.3923056; and 10.5281/zenodo.3804164).

Declarations

Conflict of interest The authors have no competing interests to declare that are relevant to the content of this article.

References

Allwine KJ, Lamb BK, Eskridge R (1992) Wintertime dispersion in a mountainous basin at Roanoke, Virginia: tracer study. J Appl Meteorol 31(11):1295–1311. https://doi.org/10.1175/1520-0450(1992)031<1295: WDIAMB>2.0.CO;2

Axelsen SL, van Dop H (2009a) Large-eddy simulation of katabatic winds. Part 1: comparison with observations. Acta Geophys 57(4):803–836

Axelsen SL, van Dop H (2009b) Large-eddy simulation of katabatic winds part 2: sensitivity study and comparison with analytical models. Acta Geophys 57(4):837–856

Ayer HS (1961) On the dissipation of drainage wind systems in valleys in morning hours. J Meteorol 18(4):560–563. https://doi.org/10.1175/1520-0469(1961)018<0560:OTDODW>2.0.CO;2

Bailey SCC, Sama MP, Canter CA, Pampolini LF, Lippay ZS, Schuyler TJ, Hamilton JD, MacPhee SB, Rowe IS, Sanders CD, Smith VG, Vezzi CN, Wight HM, Hoagg JB, Guzman MI, Smith SW (2020) University of kentucky measurements of wind, temperature, pressure and humidity in support of lapse-rate using



- multisite fixed-wing and rotorcraft unmanned aerial systems. Earth Syst Sci Data 12(3):1759–1773. https://doi.org/10.5194/essd-12-1759-2020
- Banta R, Cotton WR (1981) An analysis of the structure of local wind systems in a broad mountain basin. J Appl Meteorol 20(11):1255–1266. https://doi.org/10.1175/1520-0450(1981)020<1255:AAOTSO>2.0. CO:2
- Barbieri L, Kral ST, Bailey SCC, Frazier AE, Jacob JD, Reuder J, Brus D, Chilson PB, Crick C, Detweiler C, Doddi A, Elston J, Foroutan H, González-Rocha J, Greene BR, Guzman MI, Houston AL, Islam A, Kemppinen O, Lawrence D, Pillar-Little EA, Ross SD, Sama MP, Schmale DG, Schuyler TJ, Shankar A, Smith SW, Waugh S, Dixon C, Borenstein S, de Boer G (2019) Intercomparison of small unmanned aircraft system (SUAS) measurements for atmospheric science during the lapse-rate campaign. Sensors. https://doi.org/10.3390/s19092179
- Barr S, Orgill MM (1989) Influence of external meteorology on nocturnal valley drainage winds. J Appl Meteorol 28(6):497–517. https://doi.org/10.1175/1520-0450(1989)028<0497:IOEMON>2.0.CO;2
- Bell TM, Klein PM, Lundquist JK, Waugh S (2021) Remote-sensing and radiosonde datasets collected in the san luis valley during the lapse-rate campaign. Earth Syst Sci Data 13(3):1041–1051. https://doi.org/10.5194/essd-13-1041-2021
- Brus D, Gustafsson J, Kemppinen O, de Boer G, Hirsikko A (2021) Atmospheric aerosol, gases, and meteorological parameters measured during the lapse-rate campaign by the finnish meteorological institute and kansas state university. Earth Syst Sci Data 13(6):2909–2922. https://doi.org/10.5194/essd-13-2909-2021
- Clements WE, Archuleta JA, Hoard DE (1989b) Mean structure of the nocturnal drainage flow in a deep valley. J Appl Meteorol (1988–2005) 28(6):457–462
- Clements WE, Archuleta JA, Gudiksen PH (1989) Experimental design of the 1984 ASCOT field study. J Appl Meteorol 28(6):405–413. https://doi.org/10.1175/1520-0450(1989)028<0405:EDOTAF>2.0.CO;
- Clifton A, Daniels MH, Lehning M (2014) Effect of winds in a mountain pass on turbine performance. Wind Energy 17(10):1543–1562. https://doi.org/10.1002/we.1650
- de Boer G, Diehl C, Jacob J, Houston A, Smith SW, Chilson P, David Schmale I, G, Intrieri J, Pinto J, Elston J, Brus D, Kemppinen O, Clark A, Lawrence D, Bailey SCC, Sama MP, Frazier A, Crick C, Natalie V, Pillar-Little E, Klein P, Waugh S, Lundquist JK, Barbieri L, Kral ST, Jensen AA, Dixon C, Borenstein S, Hesselius D, Human K, Hall P, Argrow B, Thornberry T, Wright R, Kelly JT, (2020a) Development of community, capabilities, and understanding through unmanned aircraft-based atmospheric research: the LAPSE-RATE campaign. Bull Am Meteorol Soc 101(5):E684–E699. https://doi.org/10.1175/BAMS-D-19-0050 1
- de Boer G, Dixon C, Borenstein S, Lawrence DA, Elston J, Hesselius D, Stachura M, Laurence R III, Swenson S, Choate CM, Doddi A, Sesnic A, Glasheen K, Laouar Z, Quinby F, Frew E, Argrow BM (2021a) University of colorado and black swift technologies RPAS-based measurements of the lower atmosphere during lapse-rate. Earth Syst Sci Data 13(6):2515–2528. https://doi.org/10.5194/essd-13-2515-2021
- de Boer G, Houston A, Jacob J, Chilson PB, Smith SW, Argrow B, Lawrence D, Elston J, Brus D, Kemppinen O, Klein P, Lundquist JK, Waugh S, Bailey SCC, Frazier A, Sama MP, Crick C, Schmale D III, Pinto J, Pillar-Little EA, Natalie V, Jensen A (2020b) Data generated during the 2018 lapse-rate campaign: an introduction and overview. Earth Syst Sci Data 2020:1–15. https://doi.org/10.5194/essd-2020-98
- de Boer G, Waugh S, Erwin A, Borenstein S, Dixon C, Shanti W, Houston A, Argrow B (2021b) Measurements from mobile surface vehicles during the lower atmospheric profiling studies at elevation—a remotely-piloted aircraft team experiment (lapse-rate). Earth Syst Sci Data 13(1):155–169. https://doi.org/10.5194/essd-13-155-2021
- de Boer G, Waugh S, Erwin A, Borenstein S, Dixon C, Shanti W, Houston A, Argrow B (2021c) Measurements from mobile surface vehicles during the lower atmospheric profiling studies at elevation—a remotelypiloted aircraft team experiment (lapse-rate). Earth Syst Sci Data 13(1):155–169. https://doi.org/10.5194/ essd-13-155-2021
- Defant F (1951) Local winds. American Meteorological Society, Boston, pp 655–672. https://doi.org/10.1007/978-1-940033-70-9 54
- Di Sabatino S (2016) Boundary-layer atmospheric processes in mountainous terrain: results from materhorn-x. Boundary-Layer Meteorol 159(3):465–467
- Doran JC, Horst TW, Whiteman CD (1990) The development and structure of nocturnal slope winds in a simple valley. Boundary-Layer Meteorol 52(1):41–68
- Fernando HJS, Pardyjak ER (2013) Field studies delve into the intricacies of mountain weather. Eos Trans AGU 94(36):313–315. https://doi.org/10.1002/2013EO360001
- Fernando HJS, Pardyjak ER, Di Sabatino S, Chow FK, De Wekker SFJ, Hoch SW, Hacker J, Pace JC, Pratt T, Pu Z, Steenburgh WJ, Whiteman CD, Wang Y, Zajic D, Balsley B, Dimitrova R, Emmitt GD, Higgins CW,



- Hunt JCR, Knievel JC, Lawrence D, Liu Y, Nadeau DF, Kit E, Blomquist BW, Conry P, Coppersmith RS, Creegan E, Felton M, Grachev A, Gunawardena N, Hang C, Hocut CM, Huynh G, Jeglum ME, Jensen D, Kulandaivelu V, Lehner M, Leo LS, Liberzon D, Massey JD, McEnerney K, Pal S, Price T, Sghiatti M, Silver Z, Thompson M, Zhang H, Zsedrovits T (2015) The MATERHORN: unraveling the intricacies of mountain weather. Bull Am Meteorol Soc 96(11):1945–1967. https://doi.org/10.1175/BAMS-D-13-00131.1
- Fleagle RG (1950) A theory of air drainage. J Meteorol 7(3):227–232. https://doi.org/10.1175/1520-0469(1950)007<0227:ATOAD>2.0.CO;2
- Grisogono B, Axelsen SL (2012) A note on the pure katabatic wind maximum over gentle slopes. Boundary-Layer Meteorol 145(3):527–538
- Grisogono B, Jurlina T, Večenaj Güttler I (2015) Weakly nonlinear Prandtl model for simple slope flows. Q J R Meteorol Soc 141(688):883–892. https://doi.org/10.1002/qj.2406
- Gudiksen PH (1989) Categorization of nocturnal drainage flows within the brush creek valley and the variability of sigma theta in complex terrain. J Appl Meteorol 28(6):489–495
- Haiden T, Whiteman CD (2005) Katabatic flow mechanisms on a low-angle slope. J Appl Meteorol 44(1):113–126. https://doi.org/10.1175/JAM-2182.1
- Hang C, Nadeau DF, Jensen DD, Hoch SW, Pardyjak ER (2016) Playa soil moisture and evaporation dynamics during the materhorn field program. Boundary-Layer Meteorol 159(3):521–538
- Helmis CG, Papadopoulos KH (1996) Some aspects of the variation with time of katabatic flow over a simple slope. Q J R Meteorol Soc 122(531):595–610. https://doi.org/10.1002/qj.49712253103
- Islam A, Shankar A, Houston A, Detweiler C (2021) University of nebraska unmanned aerial system (UAS) profiling during the lapse-rate field campaign. Earth Syst Sci Data 13(6):2457–2470. https://doi.org/10.5194/essd-13-2457-2021
- Jensen AA, Pinto JO, Bailey SCC, Sobash RA, de Boer G, Houston AL, Chilson PB, Bell T, Romine G, Smith SW, Lawrence DA, Dixon C, Lundquist JK, Jacob JD, Elston J, Waugh S, Steiner M (2021) Assimilation of a coordinated fleet of uncrewed aircraft system observations in complex terrain: Enkf system design and preliminary assessment. Mon Weather Rev 149(5):1459–1480. https://doi.org/10.1175/MWR-D-20-0359.1
- Leone JM, Lee RL (1989) Numerical simulation of drainage flow in brush creek, colorado. J Appl Meteorol (1988–2005) 28(6):530–542
- Mahrt L, Sun J, Oncley SP, Horst TW (2014) Transient cold air drainage down a shallow valley. J Atmos Sci 71(7):2534–2544. https://doi.org/10.1175/JAS-D-14-0010.1
- Manins PC, Sawford BL (1979) A model of katabatic winds. J Atmos Sci 36(4):619–630. https://doi.org/10. 1175/1520-0469(1979)036<0619:AMOKW>2.0.CO;2
- McNider RT (1982) A note on velocity fluctuations in drainage flows. J Atmos Sci 39(7):1658–1660. https://doi.org/10.1175/1520-0469(1982)039<1658:ANOVFI>2.0.CO;2
- Monti P, Fernando HJS, Princevac M, Chan WC, Kowalewski TA, Pardyjak ER (2002) Observations of flow and turbulence in the nocturnal boundary layer over a slope. J Atmos Sci 59(17):2513–2534. https://doi. org/10.1175/1520-0469(2002)059<2513:OOFATI>2.0.CO;2
- Orgill MM, Schreck RI (1985) An overview of the ascot multi-laboratory field experiments in relation to drainage winds and ambient flow. Bull Am Meteorol Soc 66(10):1263–1277
- Orgill MM, Kincheloe JD, Sutherland RA (1992) Mesoscale influences on nocturnal valley drainage winds in western colorado valleys. J Appl Meteorol 31(2):121–141
- Papadopoulos KH, Helmis CG (1999) Evening and morning transition of katabatic flows. Boundary-Layer Meteorol 92(2):195–227. https://doi.org/10.1023/A:1002070526425
- Papadopoulos K, Helmis C, Soilemes AT, Kalogiros J, Papageorgas P, Asimakopoulos D (1997) The structure of katabatic flows down a simple slope. Q J R Meteorol Soc 123:1581–1601
- Pattantyus AK, Chiao S, Czyzyk S (2011) Improving High-Resolution Model Forecasts of Downslope Winds in the Las Vegas Valley. J Appl Meteorol Climatol 50(6):1324–1340. https://doi.org/10.1175/ 2011JAMC2586.1
- Pilie RJ, Mack EJ, Kocmond WC, Rogers CW, Eadie WJ (1975) The life cycle of valley fog. Part I: micrometeorological characteristics. J Appl Meteorol 14(3):347–363. https://doi.org/10.1175/1520-0450(1975)014<0347:TLCOVF>2.0.CO;2
- Pillar-Little EA, Greene BR, Lappin FM, Bell TM, Segales AR, de Azevedo GBH, Doyle W, Kanneganti ST, Tripp DD, Chilson PB (2021) Observations of the thermodynamic and kinematic state of the atmospheric boundary layer over the san luis valley, co, using the coptersonde 2 remotely piloted aircraft system in support of the lapse-rate field campaign. Earth Syst Sci Data 13(2):269–280. https://doi.org/10.5194/essd-13-269-2021



Pinto JO, Parsons DB, Brown WOJ, Cohn S, Chamberlain N, Morley B (2006) Coevolution of down-valley flow and the nocturnal boundary layer in complex terrain. J Appl Meteorol Climatol 45(10):1429–1449. https://doi.org/10.1175/JAM2412.1

- Pinto JO, Jensen AA, Jiménez PA, Hertneky T, Muñoz Esparza D, Dumont A, Steiner M (2021) Real-time wrf large-eddy simulations to support uncrewed aircraft system (UAS) flight planning and operations during 2018 lapse-rate. Earth Syst Sci Data 13(2):697–711. https://doi.org/10.5194/essd-13-697-2021
- Porch WM, Clements WE, Coulter RL (1991) Nighttime valley waves. J Appl Meteorol 30(2):145–156. https://doi.org/10.1175/1520-0450(1991)030<0145:NVW>2.0.CO;2
- Poulos GS, Bossert JE, McKee TB, Pielke RA (1999) The interaction of katabatic flow and mountain waves. Part I: observations and idealized simulations. J Atmos Sci 57(12):1919–1936. https://doi.org/10.1175/1520-0469(2000)057<1919:TIOKFA>2.0.CO;2
- Poulos GS, Bossert JE, McKee TB, Pielke RA (2007) The interaction of katabatic flow and mountain waves. Part II: case study analysis and conceptual model. J Atmos Sci 64(6):1857–1879. https://doi.org/10.1175/JAS3926.1
- Price JD, Vosper S, Brown A, Ross A, Clark P, Davies F, Horlacher V, Claxton B, McGregor JR, Hoare JS, Jemmett-Smith B, Sheridan P (2011) COLPEX: field and numerical studies over a region of small hills. Bull Am Meteorol Soc 92(12):1636–1650. https://doi.org/10.1175/2011BAMS3032.1
- Princevac M, Fernando HJS (2008) Morning breakup of cold pools in complex terrain. J Fluid Mech 616:99– 109. https://doi.org/10.1017/S0022112008004199
- Princevac M, Hunt JCR, Fernando HJS (2008) Quasi-steady katabatic winds on slopes in wide valleys: hydraulic theory and observations. J Atmos Sci 65(2):627–643. https://doi.org/10.1175/2007JAS2110.1
- Pypker T, Unsworth M, Lamb B, Allwine E, Edburg S, Sulzman E, Mix A, Bond B (2007) Cold air drainage in a forested valley: investigating the feasibility of monitoring ecosystem metabolism. Agric For Meteorol 145(3):149–166. https://doi.org/10.1016/j.agrformet.2007.04.016
- Sakiyama SK (1990) Drainage flow characteristics and inversion breakup in two alberta mountain valleys. J Appl Meteorol (1988–2005) 29(10):1015–1030
- Sanchez Gomez M, Lundquist JK, Klein PM, Bell TM (2021) Turbulence dissipation rate estimated from lidar observations during the lapse-rate field campaign. Earth Syst Sci Data 13(7):3539–3549. https://doi.org/ 10.5194/essd-13-3539-2021
- Sato T, Kondo J (1988) A simple model of drainage flow in a valley. Boundary-Layer Meteorol 45(4):355–369 Sun J, Oncley SP, Burns SP, Stephens BB, Lenschow DH, Campos T, Monson RK, Schimel DS, Sacks WJ, De Wekker SFJ, Lai CT, Lamb B, Ojima D, Ellsworth PZ, Sternberg LSL, Zhong S, Clements C, Moore DJP, Anderson DE, Watt AS, Hu J, Tschudi M, Aulenbach S, Allwine E, Coons T (2010) A multiscale and multidisciplinary investigation of ecosystem-atmosphere co2 exchange over the rocky mountains of colorado. Bull Am Meteorol Soc 91(2):209–230. https://doi.org/10.1175/2009BAMS2733.1
- Van Gorsel E, Vogt R, Christen A, Rotach M (2003) Low frequency temperature and velocity oscillations in katabatic winds. In: Extended Abstract Volume A, International Conference on Alpine Meteorol and MAP Meeting, pp 251–254
- Wagenbrenner NS, Forthofer JM, Lamb BK, Shannon KS, Butler BW (2016) Downscaling surface wind predictions from numerical weather prediction models in complex terrain with windninja. Atmos Chem Phys 16(8):5229–5241. https://doi.org/10.5194/acp-16-5229-2016
- Wieringa J (1992) Updating the davenport roughness classification. J Wind Eng Ind Aerodyn 41:357–368 Zardi D, Whiteman CD (2013) Diurnal mountain wind systems. Springer, Dordrecht, pp 35–119. https://doi.org/10.1007/978-94-007-4098-3_2

Publisher's Note Springer Nature remains neutral with regard to jurisdictional claims in published maps and institutional affiliations.

Springer Nature or its licensor (e.g. a society or other partner) holds exclusive rights to this article under a publishing agreement with the author(s) or other rightsholder(s); author self-archiving of the accepted manuscript version of this article is solely governed by the terms of such publishing agreement and applicable law.

